HHS Public Access

Author manuscript

Dev Biol. Author manuscript; available in PMC 2021 June 01.

Published in final edited form as:

Dev Biol. 2020 June 01; 462(1): 36–49. doi:10.1016/j.ydbio.2020.02.014.

Formation and contraction of multicellular actomyosin cables facilitate lens placode invagination

Nathalie S. Houssin[1], **Jessica B. Martin**[1], **Vincenzo Coppola**[3], **Sung Ok Yoon**[2], **Timothy F. Plageman Jr.**[1]

[1]College of Optometry, The Ohio State University, Columbus, OH, USA

[2]Department of Biological Chemistry and Pharmacology, Ohio State University, Columbus, OH, USA.,

[3]Department of Cancer Biology and Genetics, The Ohio State University, Columbus, OH, USA.

Abstract

Embryonic morphogenesis relies on the intrinsic ability of cells, often through remodeling the cytoskeleton, to shape epithelial tissues during development. Epithelial invagination is an example of morphogenesis that depends on this remodeling but the cellular mechanisms driving arrangement of cytoskeletal elements needed for tissue deformation remain incompletely characterized. To elucidate these mechanisms, live fluorescent microscopy and immunohistochemistry on fixed specimens were performed on chick and mouse lens placodes. This analysis revealed the formation of peripherally localized, circumferentially orientated and aligned junctions enriched in F-actin and MyoIIB. Once formed, the aligned junctions contract in a Rho-kinase and non-muscle myosin dependent manner. Further molecular characterization of these junctions revealed a Rho-kinase dependent accumulation of Arhgef11, a RhoA-specific guanine exchange factor known to regulate the formation of actomyosin cables and junctional contraction. In contrast, the localization of the Par-complex protein Par3, was reduced in these circumferentially orientated junctions. In an effort to determine if Par3 plays a negative role in MyoIIB accumulation, Par3-deficient mouse embryos were analyzed which not only revealed an increase in bicellular junctional accumulation of MyoIIB, but also a reduction of Arhgef11. Together, these results highlight the importance of the formation of the multicellular actomyosin cables that appear essential to the initiation of epithelial invagination and implicate the potential role of Arhgef11 and Par3 in their contraction and formation.

Introduction

Epithelial invagination is a process that contributes to the morphogenesis of several tissues in multiple species (Pearl et al., 2017). A current challenge is to define the molecular driving forces of this process in order to learn how embryonic cells generate the three-dimensional shape of an embryo. The mechanism of lens placode invagination comprises of a

coordinated process of epithelial cell morphology changes that ultimately cause the placodal tissue to bend inward and pinch off to eventually form a spherical vesicle (Chauhan et al., 2015; Cvekl and Ashery-Padan, 2014). Apical constriction or wedging of epithelial cells is thought to contribute to invagination, however, it is clear that this is not the only factor driving morphogenesis of the early lens (Muccioli et al., 2016; Plageman et al., 2010) or other invaginating epithelial tissues (Chung et al., 2017). While disrupting key genes that trigger apical constriction in the lens placode is detrimental to the overall shape of the lens vesicle, invagination still occurs (Chauhan et al., 2011; Lang et al., 2014; Plageman et al., 2011; Plageman et al., 2010). In addition to cell wedging, lens placodal cells also elongate in a circumferential, planar direction near the periphery of the lens placode (Muccioli et al., 2016). These anisotropic shape changes hint at a role for planar polarized molecular mechanisms and cell behaviors. Defining the molecular mechanisms that give rise to these cell behaviors will undoubtedly facilitate an understanding of epithelial invagination.

Although apical constriction itself appears dispensable for lens placode invagination, activation and contraction of actomyosin is absolutely required. Inhibition experiments using chemical inhibitors of the core RhoA-Rho-kinase-Myosin II pathway that ultimately prevent the contraction of actomyosin prevent invagination of the lens placode and other epithelial invaginations (Beane et al., 2006; Borges et al., 2011; Chung et al., 2017; Plageman et al., 2011; Sai et al., 2014). In this pathway, activation of the GTPase RhoA is triggered by various guanine exchange factors (RhoGEFs) which in turn activates Rho-kinase, whose activity is responsible for stimulating the contraction of actomyosin filaments (Agarwal and Zaidel-Bar, 2019; Munjal and Lecuit, 2014). An emerging mechanism that appears to be important for epithelial invagination is the contraction of supracellular actomyosin cable structures that span multiple cells and are positioned peripherally around the tissue. It is thought that coordinated contraction of these actomyosin cables facilitates the inward bending of epithelial structures but the pathways that form and activate these actomyosin cables are not well defined.

In order to uncover the mechanisms that underlie lens placode invagination, we have employed time-dependent observations of chick embryo lens morphogenesis. Fluorescent labeling of cellular junctions during the onset of invagination revealed novel cell behaviors and the formation of peripherally localized supracellular actomyosin cables along circumferentially orientated placodal cell junctions. The contraction of these cables is regulated by Rho-kinase and non-muscle myosin activity. Further molecular characterization revealed that Rho-kinase activity also regulates the planar-polarized distribution of the RhoGEF Arhgef11 and Par3, a member of the Par-complex. Analysis of Par3-deficient mouse embryos further revealed that Par3 may function by inhibiting the localization of MyoIIB and Arhgef11 to bicellular junctions. Together the data described here uncover novel aspects of lens placode invagination.

2. Materials and methods

2.1 Pard3 KO mouse line generation and maintenance.

To generate the Par3 (*Pard3*) KO mouse line a targeting vector was purchased from the KOMP consortium which has previously been used to generate Par3-deficient mice (project

ID 65445) (Landin Malt et al., 2019; Liu et al., 2018; Skarnes et al., 2011; Sultan et al., 2018). The targeting vector (KOMP-PRPGS00162_B_E11-Pard3) introduces a frame-shift mutation within the first PDZ domain disrupting all known Par3 isoforms. (Figure 7A). The vector DNA was linearized with the AsiI enzyme and prepared for ES electroporation according to standard methods. The Genetically Engineered Mouse Modeling Shared Resource of the OSUCCC electroporated the targeting vector into a hybrid 129sVC57Bl/6 cell line (S1B6). Analysis by Southern blot using a probe external to the 3' arm of the targeting vector showed about 50% of the ES clones targeted (see Figure 7B). Two targeted clones (1G8 and 1G11) were injected into blastocysts to generate chimeric mice. The primers used to detect the knock-out and wild-type alleles were 5'-GGGATCTCATGCTGGAGTTCTTCG-3' + 5'-TCCCAGCTGCTTAATCGAGGCCATCA-3' (KO) and 5'-CCAATTATCGGACTGTAGAATTGTGA-3' + 5'-AGTTACACTGGGAAGACCACCACAGT-3' (wt) using the protocol: [(95C 10 sec, 60C 25 sec, 72C 10 sec)x35]. The expected bands sizes were 591bp and 396 for the KO and Wt alleles, respectively.

2.2 Embryo culture and time-lapse imaging

To visualize embryonic lens placodes in real-time, HH stage13 chicken embryos were isolated with paper rings similar to published methods (El-Ghali et al., 2010) and incubated at 37°C for 1h with a 40uL stock solution of SiR-Actin (5μM, SC001, Cytoskeleton, Inc) on fresh albumen in a 35mm Petri dish with 1mL of M199 warmed medium for at least 1h before imaging. The head was then bisected and placed on a coverslip in a drop of M199 medium. Dots of grease are placed around the drop to protect the embryo from compression and a glass coverslip-bottomed dish (#D35–20–1.5N, Cellvis) is applied on top of it such that the lens placode faces the glass. Following incubation with SiR-Actin, the cultures were imaged with an inverted microscope (Nikon A1R or Zeiss Z1 Observer) and kept at 37°C with a heated chamber. Images were typically collected every 10 min for ~4h with an approximate 20 μm z-range (step size 0.3 μm). To inhibit Rho kinase or non-muscle myosin activity in embryonic lens placodes, HH12–13 chicken embryos were incubated at 37°C with a 50uM solution of Y27632 (EMD Millipore) or a 50uM solution of blebbistatin (EMD Millipore) in M199 media for 1.5–2h in a 12 well plate. The embryos were then fixed in 4% PFA overnight before immunolabeling.

2.3 Whole-mount embryo, immunolabeling and imaging

Fixed, whole mouse embryos isolated from time-mated females (E9.75–E10.5) or chicken embryos were rinsed three times in 0,1% Triton X100-PBS and placed into 4% milk (in 0,1% Triton X100-PBS) containing one or more of the following primary antibodies or fluorescent labels overnight at 4°C with constant rocking: rabbit-anti-β-catenin (1:500; Santa Cruz, sc-7199), mouse anti-β-catenin (1:500; BD Biosciences, 610153), rabbit anti-myosin IIb (1:500; Covance, PRB445P), mouse anti-myosin IIB (1:250; CMII 23-s, DSHB), rabbit Par3 (1:500; Millipore, #07–330), rabbit anti-Arhgef11 (1:200, Atlas Antibodies, HPA01126), rat anti- Phospho-Myosin Light Chain 2 (Ser19) (1:250, Cell Signaling Technology, 3675S), Phalloidin 488 (1:500; Invitrogen, A12379), rabbit anti-Prox1(1:1K, EMD Millipore, AB5475), and Hoechst 33342 (1:1000; Sigma, B-2261). For MyoIIB, Par3,

phospho-myosin (Ser19) and Arhgef11 labeling, embryos were subjected to antigen retrieval where they were immersed in 100mM Tris H 9.0 and placed into a bead bath for 30 min at 90°C prior to primary antibody incubation. Following three 0.1% Triton X100-PBS rinses, embryos were subsequently incubated with the appropriate Alexa Fluor (Invitrogen) secondary antibodies conjugated with a 488 or 594 fluorophore at a 1:500 dilution (in 0,1% Triton X100-PBS with 4% milk) for 1–2h under constant rocking.

Specimens were imaged using either a Zeiss Axio observer inverted microscope equipped with a widefield fluorescent light source and 40x Plan-Apochromat objective, a FV3000 Olympus or Nikon A1R confocal microscope utilizing 405nm, 488nm, and 633nm lasers (2–5% power) and a 40× EC Plan-Neofluar objective. Whole embryos were imaged at a 1024×1024 resolution with a z-range of 7–15μm and step size of 0.3μm.

2.4 Quantitative morphometric and image intensity analyses and statistics

Lens placodal cell and junction dimensional measurements: Apical circumferential and radial cell dimensions were quantified from .czi files using Zen 2012 (blue edition, Zeiss). First, five concentric rings with defined diameters at 50μm intervals (50–200μm) were drawn around the center of the placode. Using junctional labeling as guides, all cells lying on the circles were measured in two dimensions; the circumferential dimension was measured between the points its junctions crossed the circles while the radial dimension was measured between the inner and outer junctions at a point approximately half-way and perpendicular to the first line as performed previously (Muccioli et al., 2016). All measurements were compiled from seven placodes and their means and distributions calculated. To measure the relative “straightness” of junctions the distance between two tricellular junctions was measured and the actual length of ~150 bicellular junctions was traced and measured from 2–3 placodes in each experimental group using ImageJ. A ratio between these measurements was then calculated. Circumferential length of at least 60 cells lying along a 150μm diameter circle centered on the placode from 11–16 embryonic placodes from control, Y27632, and blebbistatin treated embryos were measured in the same manner as described above and their means calculated. The distance between junctionally positioned peaks of IF labelling of pMLC was measured using the Peak Finder tool in ImageJ (https://sils.fnwi.uva.nl/bcb/objectj/), an algorithm designed to measure the distance between peak intensities along a straight line. The spacing of pMLC was measured along at least 50 bicellular junctions from 3–4 placodes in the control and experimental groups and the mean distance and the population distribution of these distances were calculated. Statistical comparisons were made in the following manner: First, the Shapiro-Wilk test was used to determine if the datasets were normally distributed. Then, for the normally distributed datasets, statistical comparisons were calculated using student’s t- test ($p< 0.01$). For the non-normally distributed datasets, comparisons were statistically calculated using Mann and Whitney U tests (significance $p< 0.05$).

IF intensity quantification: The relative signal intensities along bicellular junctions of lens placodal cells were measured in ImageJ by using the measure tool that calculates the mean intensity along a line drawn along the junction. Each value was normalized by dividing each measured mean to the average non-junctional specific signal intensity found in

the middle of 10–50 cells/image. To calculate the mean relative intensity of F-actin, MyoIIB, and ZO1 along aligned vs. non-aligned junctions, 100–150 junctions lying ~60–85μm from the placodal center were measured from 5–7 placodes. Junctions were defined as aligned if they are parallel and emanate from the same multi-junctional vertex. To calculate the mean relative intensity of Arhgef11 along bicellular junctions in chick embryos, total 500–600 bicellular junctional measurements were taken ~60–85μm from the placodal center from at least 3 different embryonic placodes from the control and experimental groups. In mice, Arhgef11 and MyoIIB intensity measurements were compiled from ~350 bicellular junctions from 3 control and Par3-deficient embryos. The mean intensity of MyoIIB and Par3 was determined using a custom built algorithm in the image processing software MIPAR (Sosa et al., 2014) that measured the mean signal of individual junctions while excluding vertices. For the purposes of determining a difference between high and low MyoIIB signal, the junctions were divided into groups with less than half maximal MyoII vs. those with more than half the maximal MyoIIB signal. In chick embryos MyoIIB and Par3 intensity was measured along at least 50 peripherally localized bicellular junctions from 5 placodes. Images of placodes from 3 different embryos were analyzed. Tricellular junctional intensity of mouse and chick placodes was determined using ImageJ by centering a 1.5μm circle on >50 tricellular junctions of three distinct placodes within each experimental group.

3. Results

3.1 Time-dependent changes in chick lens placodal cell morphology.

Although apical constriction is a major driving force of epithelial invagination in some epithelial tissues, this process appears insufficient to direct this morphogenetic event in others (Chung et al., 2017). In order to uncover additional cellular mechanisms guiding lens placode invagination, we investigated cell shape changes during embryonic morphogenesis in chicken embryos. As revealed by immunofluorescent (IF) staining of fixed, whole-mounted embryos using the placodal marker Prox1 and the junctional marker β-catenin, the peripheral lens placode cells adopt an anisotropic geometry at the onset of invagination similar to what was previously observed in mouse embryos (Fig. 1A–C) (Muccioli et al., 2016). The process of invagination can be categorized into multiple stages. Stage 0 is defined as a thickened placode without any sign of invagination corresponding roughly to Hamburger Hamilton stage 12 (HH12). Stage 0 placodes are Prox1-positive and the cells are geometrically isotropic (Fig. 1A–B). Stage I is categorized by the earliest sign of invagination and adoption of anisotropic geometry of placodal cells, such that the cells are stretched in the circumferential direction (Fig. 1C). These observations were confirmed by compiling measurements of the circumferential (Fig.1F) and radial (Fig. 1G) dimensions of placodal cells and grouping them by their location (Fig. 1D). Calculating the circumferential/radial dimension ratios in each region demonstrated that the apical geometry of all placodal cells, regardless of location, is isotropic at Stage 0 due to the ratios remaining close to 1.0 (Fig. 1 E). During the transition from Stage 0 to Stage I, the central-most cells (within the 50μm diameter circle) reduce their radial and circumferential dimensions mostly isotropically (Fig E-G) but their circumferential/radial dimensional ratio significantly increases to a small degree. However, more peripheral cells (within the 100–200 μm circles) gain a larger degree of anisotropy (Fig. 1E), by elongating their circumferential dimension

(Fig.1F) and reducing their radial dimension (Fig.1G). Together, these data demonstrate conserved mechanisms in chick lens invagination with what is observed in mouse embryos.

Upon observing this process live using SiR-Actin, a fluorescent dye that specifically binds to F-actin and effectively marks cellular junctions, it was discovered that once cells adopt geometric anisotropy, it is gradually lost as they move toward the center of the placode (Fig. 1H). By calculating the distance and velocity of individual cells located in specific regions of the placode (defined in Fig. 1D), it was observed that cells originating in the more peripheral regions moved at a greater rate and for a longer distance than the more central cells (Fig. 1I). Centripetal movement is accompanied by a reduction in apical area (Fig. 1J) and a shift back towards geometric isotropy that is accomplished through the reduction in the circumferential junctional length but without a change in the radial length (Fig. 1L). In an earlier study, these subsequent changes involving the anisotropic to isotropic cell shape shift were initially unobserved in mouse embryos due to the shorter time frames used (Muccioli et al., 2016). However, upon analysis of transgenic mouse lens placodes at a later time-point expressing a fluorescently tagged E-cadherin protein (*Cdh1*^{CFP}) the gradual shift from anisotropy to isotropy was observed (Fig. 1K) and like the chick, appears to occur due to a decrease in circumferential junctional length (Fig. 1M).. Together, these observations demonstrate that at the onset of lens invagination, apical cell geometry changes in a two-step process. First, isotropic cells reduce their radial length and elongate their circumferential length to become anisotropic. Secondly, the circumferentially stretched cells undergo a reduction in their circumferential length to regain an isotropic shape (Fig. 1N). This process occurs as the cells move toward the center of the lens placode.

3.1 The lens placode is surrounded by contractile and aligned multicellular junctional arcs that are enriched in actomyosin

Because peripheral lens placodal cells contract in a circumferential direction, circumferentially orientated junctions were analyzed in more detail using whole-mount IF labeled embryos at different stages during early invagination. Upon labeling placodes for F-actin and Myosin IIB (MyoIIB), an intense signal was observed in circumferential junctions of the lens placode periphery at Stage I (Fig. 2B, E) and Stage II (Fig. 2C, F) but not at Stage 0 (Fig 2A, D). A higher magnification of these regions revealed that circumferential junctions intensely labeled with F-actin and MyoIIB aligned themselves with their neighbors progressively from stage 0 to stage II to form multicellular junctional arcs. These arcs are composed of 3 to 8 junctions on average (Fig.2B', C' E, F') that are oriented perpendicularly to the lens center and surround the lens placode periphery (Fig.2A'–F'). Importantly the emergence of these aligned junctions appear immediately before the circumferential cell dimensions shrink. The alignment and accumulation of actomyosin within these circumferential junctions also occurs in the peripheral region of mouse embryos after anisotropy generation (Fig. 2I). To quantify these observations, the junctional intensity of F-actin (Fig. 2G, J), MyoIIB (Fig. 2H, J) and ZO-1 (Fig. 2J) were measured in aligned or non-aligned, circumferentially orientated junctions. The population of cells with greater intensity values for F-actin (Fig. 2G) and MyoIIB (Fig 2H) markedly increased as did the average junctional intensity (Fig. 2J). However, ZO-1 intensity values remain similar in all junctions (Fig. 2J). Accumulation of actomyosin specifically along these apical multicellular junctions

suggests that they play a role in the contractile activity of the tissue and may influence invagination.

To determine if they are contractile, live chick lens placodes labeled with SiR-Actin were imaged during invagination. Using this marker, the aligned and actomyosin enriched multicellular junctional arcs are readily visible (Fig. 2J–K, arrowheads). Over the course of 135 minutes, existing arcs shorten their lengths as visualized from still frames with arrowheads marking the same junctional vertices (Fig. 2L). By measuring the length of these arcs over time it was observed that their shrinkage occurs in a relative smooth motion (Movie1, Fig. 2M). Combined with the observation that cells undergoing circumferential dimensional shortening are moving centripetally, these data suggest that the formation and contraction of these arcs are responsible for this cell behavior and may contribute to the progressive invagination of the tissue between stage 0 and stage II. It is hypothesized that contraction of these junctions influences invagination in a purse-string-like mechanism which causes the planar epithelial tissue to buckle (Fig. 2N) similar to what is speculated to occur during salivary gland placode invagination in *Drosophila* embryos (Roper, 2012).

3.3 Shortening of aligned multicellular junctional arcs is dependent on Rho-kinase activity and non-muscle myosin contraction.

To determine if the shortening of aligned, multicellular junctional arcs is due to pathways that regulate actomyosin contraction, live chicken embryos treated with SiR-actin were imaged before and during treatment with Y27632, a Rho kinase inhibitor that is known to inhibit actomyosin contractile activity and lens placode invagination (Borges et al., 2011; Plageman et al., 2011; Uehata et al., 1997). By displaying junctional arcs as a kymograph (Fig. 3A) or in still-frames (Fig. 3B), we observed that SiR-actin-labeled vertices move closer together before treatment as previously observed (Fig. 2L) and upon addition of Y27632 (indicated in Fig.3A and B by a black arrow) move further apart. In addition to lengthening arcs, the circumferential junctions of individual cells appeared wavy and their alignment perturbed as if the tension within the junctions was relieved upon treatment with Y27632 (Fig. 3C. vs. 3D). A similar effect was observed upon treating lens placodes with blebbistatin, another inhibitor of actomyosin contraction and lens placode invagination that affects myosin activity (Fig. 3E) (Borges et al., 2011; Lang et al., 2014; Straight et al., 2003). To quantify the effect on individual cells the linear index of individual circumferential junctions was calculated by determining the ratio of the distance between two vertices and the total length of the junction. An index close to 1.0 indicates a straight junction while larger values indicate a greater degree of waviness (Fig. 3F). In both treatment groups the waviness of junctions significantly increases (Fig. 3F) as does their individual length (Fig. 3G).

Interestingly, upon immunolabeling placodes with a phospho-specific antibody for myosin light chain (hereafter pMLC) a punctate arrangement decorating the apical junctions is observed (Fig. 4A–B). This pattern is reminiscent of the sarcomeric-like bipolar filament arrangement observed in other non-muscle cells (Choi et al., 2016; Dasbiswas et al., 2018; Ebrahim et al., 2013; Fenix et al., 2016). Because the phosphorylated epitope resides near the head region of the MyoIIB protein complex it is possible that the distance between these

spots may indicate the degree of actomyosin contraction in a localized region. To test this possibility, radial and circumferential junctions of late Stage 0 lens placodal cells were imaged with the pMLC antibody (Fig. 4A) and the distance between spots was measured using an ImageJ algorithm (Peak Finder) which automatically calculates the distance between peaks of intensity (Fig. 4C–D). At this stage it is expected that the radially orientated junctions are under more tension, due to their decreasing length at this stage (Fig. 1L), than the circumferentially orientated junctions and will have closer pMLC peaks. Indeed, the population of measurements along the radial junctions tended to have a larger proportion of peaks closer together than the circumferential junctions (Fig. 4E). The analysis was repeated on Y27632 treated placodes to determine if these peak distances increase in the presence of an actomyosin tension inhibitor. Unlike the control, the peak distances between pMLC puncta in radially vs. circumferentially orientated junctions are approximately the same (Fig. 4F). This was due to an increase in the radially orientated junctions and the circumferentially orientated junctional peak distances did not significantly change (Fig. 4G). Because the peak distances are closer together in junctions that are contracting and that they increase in the presence of Y27632 it suggests that this attribute is a good marker for actomyosin contractility. Because the circumferential junctions contract following anisotropy generation and actomyosin accumulation, we hypothesized that pMLC puncta would be closer together along these junctions during contraction. When observing aligned circumferential junctions that are presumably contracting, we noticed regions of widely spaced pMLC puncta potentially indicating a relaxed state, but other regions where the pMLC puncta were closer together (Fig. 4H–I). Given this observation it is likely that as these aligned junctional arcs contract in some junctions but not others, an attribute we observed during live imaging of SiR-Actin treated embryos (Fig. 2K & 2L).

3.4: Arhgef11 localization to aligned, circumferentially-orientated junctions in the lens placode is Rho-kinase-dependent

A candidate approach was next undertaken to identify proteins that may trigger the activation of the circumferentially orientated multicellular junctional arcs. Arhgef11 is a known activator of RhoA, a small GTPase known to regulate actomyosin contractility in the lens placode (Borges et al., 2011; Plageman et al., 2011). Furthermore, Arhgef11 function has previously been linked to junctional contraction in embryonic epithelial invagination and neural tube closure in the chick (Nishimura et al., 2012; Sai et al., 2014).). Upon immunolabeling of in Stage I lens placodes, it was observed that Arhgef11 is enriched in circumferentially orientated, aligned junctional arcs (Fig. 5A, closed arrowheads), but often absent from radially orientated junctions (Fig. 5A open arrowheads)

In the presence of the Rho-kinase inhibitor, it was observed that this enrichment is attenuated and that the signal appears more evenly distributed among all junctions regardless of their orientation or alignment (Fig. 5B). When the junctional signal intensity is correlated with the orientation of the junction, it was observed that the mean signal intensity is greater among the junctions orientated more circumferentially in control treated embryos and that this correlation is eliminated in the presence of Y27632 (Fig. 5C vs. 5D). The average intensity along all junctions is also increased (Fig. 5E). Arhgef11 also appears enriched in tricellular and multi-cellular junctions and that this enrichment is attenuated upon Y27632

treatment (Fig. 5F–G). This result was confirmed upon signal intensity quantification and the average is significantly decreased when Rho-kinase in inhibited (Fig. 5H–I). To determine if Arhgef11 may be involved in junctional contractility its localization along bicellular junctions was observed simultaneously with pMLC at high magnification (Fig. 5J–L). Interestingly, among aligned circumferential junctions with intense Arhgef11 signal, the pMLC spots often appear closer together (Fig. 5L–M, arrowheads). This result is consistent with our model in which the circumferential junctions contract during stage I. The preferential distribution (or redistribution) of Arhgef11 along the circumferential junctions is thought to facilitate the actomyosin contraction. This stands in contrast to the absence of Arhgef11 in many radial and non-aligned circumferential junctions (Fig. 5J–K) and in regions of less intense Arhgef11 signal along aligned circumferential junctions (arrows Fig. 5L–M). The density of pMLC spots in the presence of Arhgeff11 may be indicative of an ability to induce actomyosin contractility.

3.5 Par3 restricts the accumulation of contractile MyoIIB and Arhgef11 to bicellular placodal junctions

Par3 and members of the Par complex are known to inhibit junctional contractility (Ishiuchi and Takeichi, 2011) and the *Drosophila* Par3-homolog, bazooka, is anisotropically localized in epithelial tissues undergoing morphogenesis (Simoes Sde et al., 2010). To determine if Par3 plays a similar role in the lens placode, Par3 and MyoIIb co-immunolabeling was performed (Fig. 6A–B). Intensity measurements along junctions demonstrated that in much of the placode Par3 localization was isotropically localized, but in cells that lie along the circumferentially orientated aligned junctions, Par3 localization was anisotropic (Fig. 6C). An analysis of Par3 and myoIIB distributions at high magnification along aligned circumferential junctions revealed that Par3 labeling intensity is often reduced where MyoIIB is accumulated (arrowheads Fig. 6D). To confirm this correlation, IF labeling intensity of MyoIIB and Par3 were simultaneously measured along bicellular apical junctions and an inverse correlation was observed (Fig. 6E). The mean intensity of Par3 was significantly greater among junctions with the lowest MyoIIB labeling (~1.2 fold, $p<0.05$) suggesting that Par3 could be limiting the accumulation of junctional MyoIIB in junctional arcs. To determine if Par3 may also be inhibitory to junctional contractility in the chick lens placode, pMLC and Par3 were co-labeled and analyzed at high magnification. In contrast to Arhgef11, Par3 was reduced in radial junctions (Fig. 6E) and regions of aligned circumferential junctions (arrowheads, Fig. 6G–H) where pMLC spots appear close together and more prominent in non-aligned circumferential junctions and in aligned circumferential junctions where the pMLC spots are further apart (arrows Fig. 6G–H). To test more directly if Par3 regulates MyoIIB accumulation, Par3 deficient mouse embryos were generated (Fig 7A–B) and were verified for loss of protein at Stage I). by immunolabeling lens placodes for Par3 and ZO-1 (Fig 7C and 7D). As expected, the protein is no longer observed along the apical junctions (Fig 7C’ and 7 D’) marked by the localization of ZO-1 (Fig 7C” and 7 D”). Homozygous mutant embryos also displayed an embryonic lethal heart phenotype identical to what was observed previously supporting the utility of this line (Hirose et al., 2006). Quantification of MyoIIB labeling in placodal junctions of Par3 deficient mouse embryos confirmed that there is a significant increase in the levels of MyoIIB (Fig. 7E–F and 7E’–F’ and graph 7G).

Because MyoIIB and Arhgef11 are both strongly localized to aligned circumferential junctions, and that Par3 may restrict MyoIIB to junctions, the effect on Arhgef11 localization was analyzed in the absence of Par3. Like in chick embryos, Arhgef11 is localized to many but not all circumferentially orientated junctions in mouse lens placodes (arrowheads, Fig. 8A). However, in the absence of Par3 the accumulation to any bicellular junctions appears reduced and anisotropic localization is lost (arrowheads, Fig. 8B). Interestingly localization of Arhgef11 to tricellular junctions appeared increased in the absence of Par3 (Fig. 8C. vs. 8D). Quantification of bicellular and tricellular junctional localization confirmed this shift in Arhgef11 localization in the absence of Par3 such that the bicellular junctional intensity was significantly reduced (Fig 8E–F) and the tricellular junctional intensity was significantly enhanced (Fig. 8G–H).

Discussion

4.1. Summary of Results

At the onset of invagination, cells in the periphery of the chick lens placode alter their shape such that they reduce their radial junctional length and elongate their circumferential junctions, a result similar to what we previously observed in mouse embryos (Muccioli et al., 2016). However, these data also show that following this shape change, an accumulation of actomyosin occurs specifically along circumferential junctions that align with junctions of neighboring cells. Despite their recent expansion, these junctions will subsequently shorten in concert with their neighbors in a Rho-kinase and non-muscle myosin-dependent manner. As the circumferentially orientated actomyosin cables contract, cells move toward the center of the placode. It is speculated that the contraction of actomyosin arcs and possibly the centripetal movement of cells facilitate the initial bending of the placode during lens invagination. The purse-string like contraction surrounding the placode is thought to cause buckling of the planar epithelium in a manner akin to column buckling, a phenomenon observe when a compressive force is applied to a column (Yoo and Lee, 2011). Rather than this occurring in a linear direction, placodal morphogenesis is hypothesized to initiate as a bulge-like buckle in the epithelial plane.

In an effort to identify potential molecules important for inducing contraction, Arhgef11 localization was analyzed. Arhgef11 appears preferentially localized to circumferentially orientated junctions in the peripheral lens placode and is concentrated in regions where the actomyosin is contracted. In addition, the distribution of Arhgef11 itself appears to be dependent on Rho-kinase activity and its anisotropic localization along bicellular junctions is lost. In contrast to Arhgef11, a core member of the Par-complex, Par3, appears to have an inverse localization pattern with MyoIIB and its localization is reduced in junctions where actomyosin is contracting. The increased localization of MyoIIB to bicellular junctions in the absence of Par3 from mouse lens placodes further supports a role for Par3 to restrict actomyosin accumulation in junctions. Par3’s ability to regulate the activation of actomyosin is also supported by the mislocalization of Arhgef11 away from bicellular junctions in Par3 mutant mouse placodes.

4.2 Cell geometry changes at the onset of invagination

The cell shape changes observed between Stage 0/I to generate anisotropy in the peripheral lens placode at the onset of invagination in the chick are similar to those observed in mouse embryos (Muccioli et al., 2016), suggesting conserved mechanisms of morphogenesis. The triggering events that cause peripheral placodal cells to stretch in the circumferential direction is not immediately clear, but our previous results suggest that junctional shortening of radial junctions could be due to anisotropic localization and function of Shroom3, p120-catenin, and a local accumulation of actomyosin and elongation could be due to an inhibition of these pathways mediated by Cdc42 and the Par complex(Muccioli et al., 2016). This possibility is strengthened here by the observation that pMLC-positive puncta along junctions, which may be representative of the sarcomeric like subunits of non-muscle myosin (Choi et al., 2016; Coravos and Martin, 2016; Ebrahim et al., 2013), are closer together in radial junctions vs. circumferential junctions and that this is attenuated by Rho-kinase inhibition. The change in shape of these cells is reminiscent of what occurs in epithelial tumors or clonal populations within epithelia where the mitotic rate is higher within the clone/tumor vs. the surrounding cells (Legoff et al., 2013; Levayer, 2019; Mao et al., 2013). In these scenarios, the elevated mitotic rate places an outward force within the clone or tumor pushing on the peripheral-most cells and inducing their anisotropic shape. Whether lens placodal cells stretch in response to a mechanical cue was not tested. However, if they do it may be independent of an elevated mitotic rate because the tritiated thymidine labeling index of the chick lens placode and the surrounding tissue are similar (Zwaan and Pearce, 1971). Rather, placodal thickening itself and/or placodal extracellular matrix deposition may contribute to a possible mechanical cue, processes that have been suggested to facilitate lens invagination (Huang et al., 2011)

4.2. Formation and contraction of circumferentially orientated actomyosin cables of the lens placode

A major observation made in this study was the formation and contraction of actomyosin cables near the periphery of the lens placode that form along aligned circumferentially orientated bicellular junctions at the onset of invagination. Because these structures form at the onset of invagination and persist as invagination proceeds it is posited that they are likely a primary driving force for this morphogenetic event. Inhibition of either Rho-kinase activity or non-muscle myosin activation completely halts lens placode invagination possibly because the process of actomyosin cable contraction is inhibited (Borges et al., 2011; Plageman et al., 2011). Importantly, the contraction of circumferential actomyosin cables may partially or wholly explain why lens placodes invaginate when apical constriction is significantly attenuated (Lang et al., 2014; Plageman et al., 2011; Plageman et al., 2010). It also suggests that although Rho-kinase and non-muscle myosin activity regulate both apical constriction and actomyosin cable contraction the mechanisms that trigger contraction may be distinct.

The formation and contraction of actomyosin cables are also known to shape several embryonic epithelial tissues such as the vertebrate neural tube (McGreevy et al., 2015; Nishimura et al., 2012) and several morphogenetic events in *Drosophila* including dorsal closure (Chang et al., 2011; Kaltschmidt et al., 2002), germband extension (Simoes Sde et

al., 2010), boundary formation of wing discs (Major and Irvine, 2006) and parasegments (Monier et al., 2010). Invagination of *Drosophila* tracheal and salivary placodes are also accompanied by circumferentially orientated apical junctions enriched in actomyosin (Nishimura et al., 2007; Roper, 2012). The formation of actomyosin cables in the tracheal placode was suggested to be a result of differential EGFR activity along the tracheal placode border promoting non-muscle myosin accumulation at the junctional interface (Nishimura et al., 2007). In the salivary gland placode, distinct expression levels of the apical-basal polarity and Par-complex regulating protein Crumbs (Bazellieres et al., 2009; Pichaud, 2018) in placodal vs. non-placodal cells leads to anisotropic accumulation of myosin in the surrounding actomyosin cable (Roper, 2012). Whether similar mechanisms are shared with the lens placode is a subject of ongoing investigation.

Because of its preferential localization to circumferentially orientated junctions of the peripheral lens placode, Arhgef11 is an intriguing candidate for instigating the contraction of the actomyosin cables. Arhgef11 is known to both activate RhoA and recruit MyoIIB to apical junctions (Itoh, 2013; Rumenapp et al., 1999) and it is possible that Arhgef11 functions to do the same thing along the peripheral circumferential junctions of the lens placode. If the spacing between the pMLC puncta observed along junctions is indicative of contraction, then the preferential localization of Arhgef11 to puncta that are positioned closer together supports this notion. Reduced expression of Arhgef11 during otic placode invagination and neural tube closure causes a reduction in apical constriction and actomyosin cable orientation also points to a role in regulating junctional contraction in epithelial morphogenesis (Nishimura et al., 2012; Sai et al., 2014). The data presented here also show that both the anisotropic bicellular junctional localization of Arhgef11 and tricellular junctional localization is dependent on Rho-kinase. Therefore, Rho-kinase activity may be both up and downstream of Arhgef11. One explanation for the loss of anisotropic localization in bicellular junctions could be that Arhgef11 protein normally localizing to tricellular junctions becomes ectopically redistributed to non-enriched bicellular junctions. A feedback loop may be in place that reinforces Rho-kinase dependent localization of Arhgef11 in places where it is stimulating contraction. Rho-kinase participation in other feedback loops that regulate its activity and actomyosin cable formation are known (Mori et al., 2009; Ong et al., 2019) and may be similarly occurring in the lens placode.

In addition to its other roles regulating apical-basal polarity and cell division orientation (Chen and Zhang, 2013; Vorhagen and Niessen, 2014), the Par-complex has also been implicated in the formation of supracellular actomyosin cables. Specifically, planar polarized localization of Par3 and aPKC, both core components of the Par-complex, are thought to have an inhibitory role in regulating their formation (Major and Irvine, 2006; Roper, 2012; Simoes Sde et al., 2010). Reduced Par3 localization in the actomyosin rich peripheral circumferential junctions, inverse correlation of Par3 with more densely arranged pMLC puncta, and an increase in junctional MyoIIB in the absence of lens placodal Par3 are all consistent with these observations. Curiously, the absence of Par3 also induced an increase of tricellular junctional localization of Arhgef11 while decreasing its bicellular localization. This result is exactly the opposite of what was observed in the presence of the Rho-kinase inhibitor. Given that Par3 can inhibit Rho-kinase function (Ishiuchi and Takeichi, 2011), a

possible explanation for this could be that Rho-kinase activity modulates Arhgef11 localization to tricellular junctional structures at the expense of its bicellular localization.

Together, these data provide new insight into how the lens placode invaginates which is likely similar to other tissues undergoing morphogenesis. Although not tested here, it is speculated that the mechanical environment of placodal cells triggers the formation of actomyosin cables in an effort to mitigate local tissue stress, similar to mechanisms recently proposed from experiments performed on *Drosophila* wing discs (Duda et al., 2019). Future efforts will be focused on determining the location of cellular stresses, how actomyosin cables are coordinately linked to neighboring cells, and what instigates their formation.

Supplementary Material

Refer to Web version on PubMed Central for supplementary material.

Acknowledgements:

The authors would like to thank the efforts of Kenneth Herman and GEMMC facility and staff for generation and maintenance of the Pard3 KO mouse line. (P30 CA016058) and Sara Cole and the OSU Campus Microscopy and Imaging Facility for microscopy instrument use and guidance (P30CA016058). The research reported here was supported by the National Eye Institute of the National Institutes of Health under award number R01EY026910 (NH and TP).

References:

Agarwal P, Zaidel-Bar R, 2019 Principles of Actomyosin Regulation In Vivo. Trends Cell Biol 29, 150–163. [PubMed: 30385150]

Bazellieres E, Assemat E, Arsanto JP, Le Bivic A, Massey-Harroche D, 2009 Crumbs proteins in epithelial morphogenesis. Frontiers in bioscience 14, 2149–2169.

Beane WS, Gross JM, McClay DR, 2006 RhoA regulates initiation of invagination, but not convergent extension, during sea urchin gastrulation. Developmental biology 292, 213–225. [PubMed: 16458878]

Borges RM, Lamers ML, Forti FL, Santos MF, Yan CY, 2011 Rho signaling pathway and apical constriction in the early lens placode. Genesis 49, 368–379. [PubMed: 21309072]

Chang LH, Chen P, Lien MT, Ho YH, Lin CM, Pan YT, Wei SY, Hsu JC, 2011 Differential adhesion and actomyosin cable collaborate to drive Echinoid-mediated cell sorting. Development 138, 3803–3812. [PubMed: 21795280]

Chauhan B, Plageman T, Lou M, Lang R, 2015 Epithelial morphogenesis: the mouse eye as a model system. Current topics in developmental biology 111, 375–399. [PubMed: 25662266]

Chauhan BK, Lou M, Zheng Y, Lang RA, 2011 Balanced Rac1 and RhoA activities regulate cell shape and drive invagination morphogenesis in epithelia. Proceedings of the National Academy of Sciences of the United States of America 108, 18289–18294. [PubMed: 22021442]

Chen J, Zhang M, 2013 The Par3/Par6/aPKC complex and epithelial cell polarity. Exp Cell Res 319, 1357–1364. [PubMed: 23535009]

Choi W, Acharya BR, Peyret G, Fardin MA, Mege RM, Ladoux B, Yap AS, Fanning AS, Peifer M, 2016 Remodeling the zonula adherens in response to tension and the role of afadin in this response. The Journal of cell biology 213, 243–260. [PubMed: 27114502]

Chung S, Kim S, Andrew DJ, 2017 Uncoupling apical constriction from tissue invagination. Elife 6.

Coravos JS, Martin AC, 2016 Apical Sarcomere-like Actomyosin Contracts Nonmuscle Drosophila Epithelial Cells. Developmental cell 39, 346–358. [PubMed: 27773487]

Cvekl A, Ashery-Padan R, 2014 The cellular and molecular mechanisms of vertebrate lens development. Development 141, 4432–4447. [PubMed: 25406393]

Dasbiswas K, Hu S, Schnorrer F, Safran SA, Bershadsky AD, 2018 Ordering of myosin II filaments driven by mechanical forces: experiments and theory. Philos Trans R Soc Lond B Biol Sci 373.

Duda M, Kirkland NJ, Khalilgharibi N, Tozluoglu M, Yuen AC, Carpi N, Bove A, Piel M, Charras G, Baum B, Mao Y, 2019 Polarization of Myosin II Refines Tissue Material Properties to Buffer Mechanical Stress. Developmental cell 48, 245–260 e247. [PubMed: 30695698]

Ebrahim S, Fujita T, Millis BA, Kozin E, Ma X, Kawamoto S, Baird MA, Davidson M, Yonemura S, Hisa Y, Conti MA, Adelstein RS, Sakaguchi H, Kachar B, 2013 NMII forms a contractile transcellular sarcomeric network to regulate apical cell junctions and tissue geometry. Current biology : CB 23, 731–736. [PubMed: 23562268]

El-Ghali N, Rabadi M, Ezin AM, De Bellard ME, 2010 New methods for chicken embryo manipulations. Microsc Res Tech 73, 58–66. [PubMed: 19582831]

Fenix AM, Taneja N, Buttler CA, Lewis J, Van Engelenburg SB, Ohi R, Burnette DT, 2016 Expansion and concatenation of nonmuscle myosin IIA filaments drive cellular contractile system formation during interphase and mitosis. Molecular biology of the cell 27, 1465–1478.

Hirose T, Karasawa M, Sugitani Y, Fujisawa M, Akimoto K, Ohnos S, Noda T, 2006 PAR3 is essential for cyst-mediated epicardial development by establishing apical cortical domains. Development 133, 1389–1398. [PubMed: 16510507]

Huang J, Rajagopal R, Liu Y, Dattilo LK, Shaham O, Ashery-Padan R, Beebe DC, 2011 The mechanism of lens placode formation: a case of matrix-mediated morphogenesis. Developmental biology 355, 32–42. [PubMed: 21540023]

Ishiuchi T, Takeichi M, 2011 Willin and Par3 cooperatively regulate epithelial apical constriction through aPKC-mediated ROCK phosphorylation. Nature cell biology 13, 860–866. [PubMed: 21685893]

Itoh M, 2013 ARHGEF11, a regulator of junction-associated actomyosin in epithelial cells. Tissue Barriers 1, e24221. [PubMed: 24665387]

Kaltschmidt JA, Lawrence N, Morel V, Balayo T, Fernandez BG, Pelissier A, Jacinto A, Martinez Arias A, 2002 Planar polarity and actin dynamics in the epidermis of Drosophila. Nature cell biology 4, 937–944. [PubMed: 12447392]

Landin Malt A, Dailey Z, Holbrook-Rasmussen J, Zheng Y, Hogan A, Du Q, Lu X, 2019 Par3 is essential for the establishment of planar cell polarity of inner ear hair cells. Proceedings of the National Academy of Sciences of the United States of America 116, 4999–5008. [PubMed: 30814219]

Lang RA, Herman K, Reynolds AB, Hildebrand JD, Plageman TF Jr., 2014 p120-catenin-dependent junctional recruitment of Shroom3 is required for apical constriction during lens pit morphogenesis. Development 141, 3177–3187. [PubMed: 25038041]

Legoff L, Rouault H, Lecuit T, 2013 A global pattern of mechanical stress polarizes cell divisions and cell shape in the growing Drosophila wing disc. Development 140, 4051–4059. [PubMed: 24046320]

Levayer R, 2019 Solid stress, competition for space and cancer: The opposing roles of mechanical cell competition in tumour initiation and growth. Semin Cancer Biol.

Liu WA, Chen S, Li ZZ, Lee CH, Mirzaa G, Dobyns WB, Ross ME, Zhang JY, Shi SH, 2018 PARD3 dysfunction in conjunction with dynamic HIPPO signaling drives cortical enlargement with massive heterotopia. Genes & development 32, 763–780. [PubMed: 29899142]

Major RJ, Irvine KD, 2006 Localization and requirement for Myosin II at the dorsal-ventral compartment boundary of the Drosophila wing. Developmental dynamics : an official publication of the American Association of Anatomists 235, 3051–3058. [PubMed: 17013876]

Mao Y, Tournier AL, Hoppe A, Kester L, Thompson BJ, Tapon N, 2013 Differential proliferation rates generate patterns of mechanical tension that orient tissue growth. The EMBO journal 32, 2790–2803. [PubMed: 24022370]

McGreevy EM, Vijayraghavan D, Davidson LA, Hildebrand JD, 2015 Shroom3 functions downstream of planar cell polarity to regulate myosin II distribution and cellular organization during neural tube closure. Biology open 4, 186–196. [PubMed: 25596276]

Monier B, Pelissier-Monier A, Brand AH, Sanson B, 2010 An actomyosin-based barrier inhibits cell mixing at compartmental boundaries in Drosophila embryos. Nature cell biology 12, 60–69. [PubMed: 19966783]

Mori K, Amano M, Takefuji M, Kato K, Morita Y, Nishioka T, Matsuura Y, Murohara T, Kaibuchi K, 2009 Rho-kinase Contributes to Sustained RhoA Activation through Phosphorylation of p190A RhoGAP. Journal of Biological Chemistry 284, 5067–5076. [PubMed: 19103606]

Muccioli M, Qaisi D, Herman K, Plageman TF Jr., 2016 Lens placode planar cell polarity is dependent on Cdc42-mediated junctional contraction inhibition. Developmental biology 412, 32–43. [PubMed: 26902112]

Munjal A, Lecuit T, 2014 Actomyosin networks and tissue morphogenesis. Development 141, 1789–1793. [PubMed: 24757001]

Nishimura M, Inoue Y, Hayashi S, 2007 A wave of EGFR signaling determines cell alignment and intercalation in the Drosophila tracheal placode. Development 134, 4273–4282. [PubMed: 17978004]

Nishimura T, Honda H, Takeichi M, 2012 Planar cell polarity links axes of spatial dynamics in neural-tube closure. Cell 149, 1084–1097. [PubMed: 22632972]

Ong K, Collier C, DiNardo S, 2019 Multiple feedback mechanisms fine-tune Rho signaling to regulate morphogenetic outcomes. Journal of cell science 132.

Pearl EJ, Li J, Green JB, 2017 Cellular systems for epithelial invagination. Philos Trans R Soc Lond B Biol Sci 372.

Pichaud F, 2018 PAR-Complex and Crumbs Function During Photoreceptor Morphogenesis and Retinal Degeneration. Front Cell Neurosci 12, 90. [PubMed: 29651238]

Plageman TF Jr., Chauhan BK, Yang C, Jaudon F, Shang X, Zheng Y, Lou M, Debant A, Hildebrand JD, Lang RA, 2011 A Trio-RhoA-Shroom3 pathway is required for apical constriction and epithelial invagination. Development 138, 5177–5188. [PubMed: 22031541]

Plageman TF Jr., Chung MI, Lou M, Smith AN, Hildebrand JD, Wallingford JB, Lang RA, 2010 Pax6-dependent Shroom3 expression regulates apical constriction during lens placode invagination. Development 137, 405–415. [PubMed: 20081189]

Roper K, 2012 Anisotropy of Crumbs and aPKC drives myosin cable assembly during tube formation. Developmental cell 23, 939–953. [PubMed: 23153493]

Rumenapp U, Blomquist A, Schworer G, Schablowski H, Psoma A, Jakobs KH, 1999 Rho-specific binding and guanine nucleotide exchange catalysis by KIAA0380, a dbl family member. FEBS Lett 459, 313–318. [PubMed: 10526156]

Sai X, Yonemura S, Ladher RK, 2014 Junctionally restricted RhoA activity is necessary for apical constriction during phase 2 inner ear placode invagination. Developmental biology 394, 206–216. [PubMed: 25173873]

Simoes Sde M, Blankenship JT, Weitz O, Farrell DL, Tamada M, Fernandez-Gonzalez R, Zallen JA, 2010 Rho-kinase directs Bazooka/Par-3 planar polarity during Drosophila axis elongation. Developmental cell 19, 377–388. [PubMed: 20833361]

Skarnes WC, Rosen B, West AP, Koutsourakis M, Bushell W, Iyer V, Mujica AO, Thomas M, Harrow J, Cox T, Jackson D, Severin J, Biggs P, Fu J, Nefedov M, de Jong PJ, Stewart AF, Bradley A, 2011 A conditional knockout resource for the genome-wide study of mouse gene function. Nature 474, 337–U361. [PubMed: 21677750]

Sosa JM, Huber DE, Welk B, Fraser HL, 2014 Development and application of MIPAR™: a novel software package for two- and three-dimensional microstructural characterization. Integrating Materials and Manufacturing Innovation 3, 123–140.

Straight AF, Cheung A, Limouze J, Chen I, Westwood NJ, Sellers JR, Mitchison TJ, 2003 Dissecting temporal and spatial control of cytokinesis with a myosin II Inhibitor. Science 299, 1743–1747. [PubMed: 12637748]

Sultan KT, Liu WA, Li ZL, Shen ZF, Li ZZ, Zhang XJ, Dean O, Ma J, Shi SH, 2018 Progressive divisions of multipotent neural progenitors generate late-born chandelier cells in the neocortex. Nature Communications 9.

Uehata M, Ishizaki T, Satoh H, Ono T, Kawahara T, Morishita T, Tamakawa H, Yamagami K, Inui J, Maekawa M, Narumiya S, 1997 Calcium sensitization of smooth muscle mediated by a Rho-associated protein kinase in hypertension. Nature 389, 990–994. [PubMed: 9353125]

Vorhagen S, Niessen CM, 2014 Mammalian aPKC/Par polarity complex mediated regulation of epithelial division orientation and cell fate. Exp Cell Res 328, 296–302. [PubMed: 25128813]

Yoo CH, Lee SC, 2011 Buckling of Columns. Stability of Structures: Principles and Applications, 1–73.

Zwaan J, Pearce TL, 1971 Cell population kinetics in the chicken lens primordium during and shortly after its contact wth the optic cup. Developmental biology 25, 96–118. [PubMed: 5557971]

Highlights:

- Chick and mouse lens placode invagination involves the contraction of multicellular actomyosin cables peripherally surrounding the tissue
- Contraction of these cables are Rho-kinase and non-muscle myosin dependent and are enriched with Arhgef11
- Pseudo-sarcomeric repeat like-structures effectively mark the contraction state of bicellular junctions in the lens placode
- Reduction of Par3 facilitates bicellular myosin localization and actomyosin cable formation

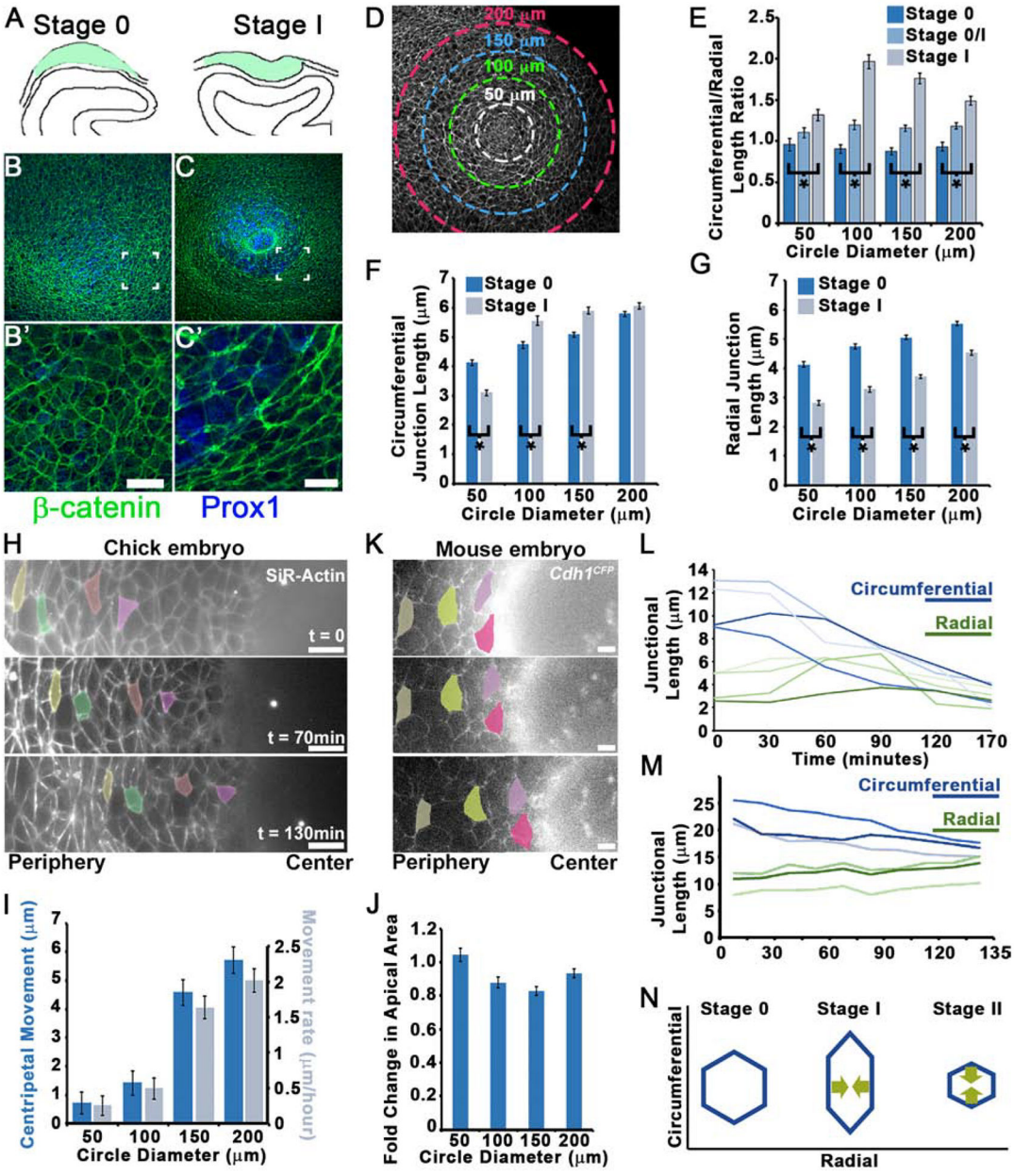

Fig. 1. A)

Drawings of cross sections of the corresponding lens invagination. The green area corresponds to the lens placode (B-C) Immunofluorescent labeling of whole mount wild type chicken embryos with β-catenin (green) and Prox1(blue), a specific lens cell marker, before (stage 0) and at the onset of invagination (stage I). The white squared regions indicate the regions magnified in B'-C'. D) Diagram of the region where cell measurements were made. E-G) Graphs indicating the average cellular junction length ratio (E), the circumferential (F), or radial dimensions (G) lying along circles drawn at four distances (D) from the center of the placode at Stage 0, 0/I, and/or Stage I. H and K) Still frames at three time-points from a time-lapse movie of a chick lens placode labeled with SiR-Actin (H) and a mouse lens placode expressing Cadherin 1-CFP (Cdh $^{cfp/cfp}$) (K). Four pseudo-colored

cells are highlighted to show their migration toward the center and changes in shape. I) the graph indicates the mean distance and rate of centripetal movement of cells initially lying at distinct distances from the center. J) The graph represents the apical area fold change of placodal cells located at four distances from the center. L &M) Variations of circumferential and radial junctional length of representative individual placodal cells during epithelial invagination in the chick (L) and the mouse (M). N) The diagram depicts the radial and circumferential junctional length rearrangements between stage 0 and stage II. The green arrows indicate the dimension predominantly shortening. Scale bars=10 μm. Error bars show the standard error and the asterisks indicate $p<0.01$ (Studentt-test) or $p<\alpha= 0.05$(MW U test).

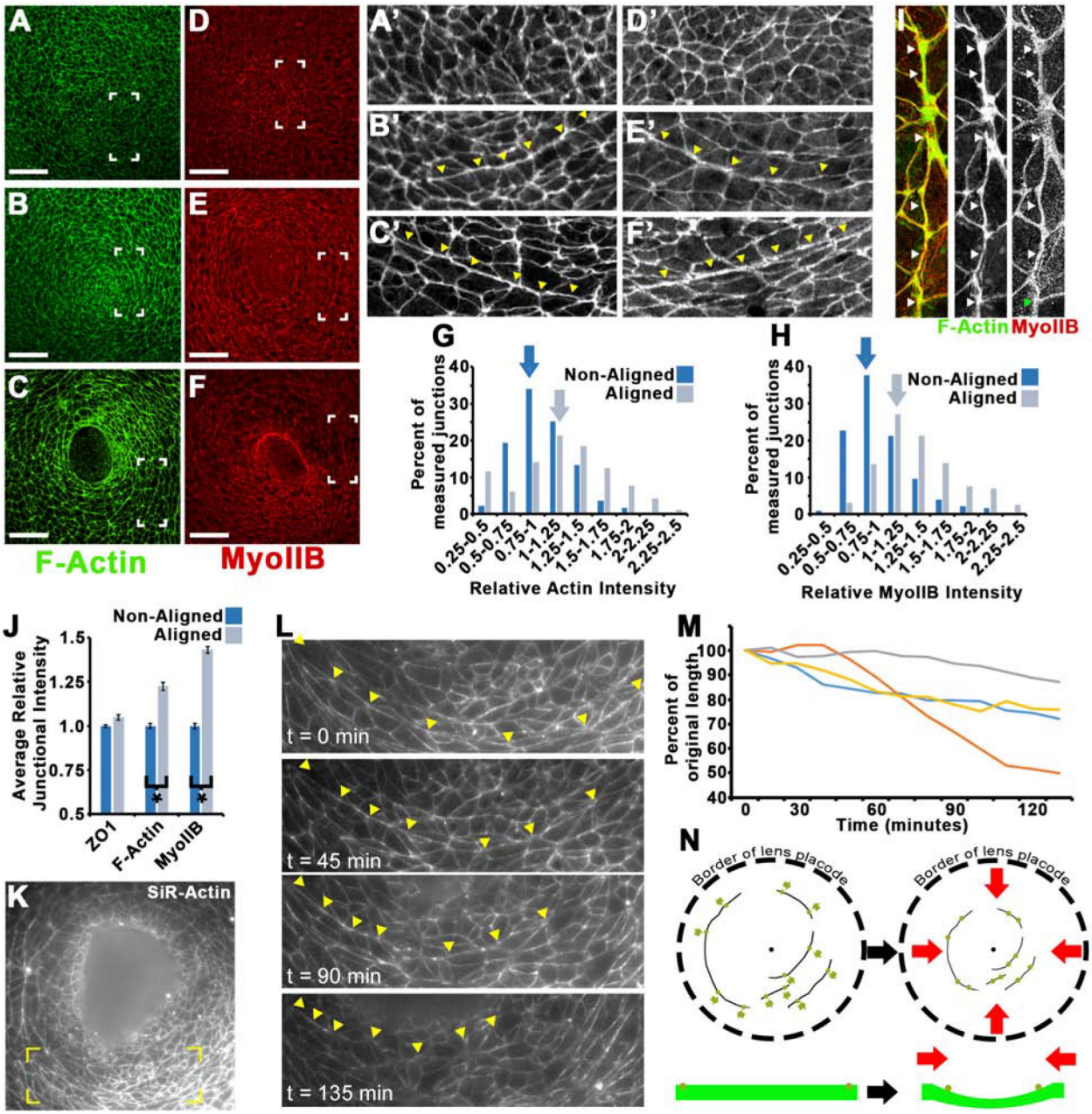

Fig. 2.

(A-F) F-actin and MyoIIB immunofluorescent labeling of whole mount wild type chicken embryos at three distinct lens invagination stages (A-D: stage 0; B-E: stage I; C-F: stage II). The white rectangular regions are magnified in the adjacent panels (A'-F'). Note that circumferential junctions align from stage 0 (A'-D')to stage II (C'-F') forming multicellular arcs (yellow arrowheads). (G-H) The graphs indicate the population distribution of signal intensities among all measured junctions labeled for F-Actin (G) and MyoIIB (H) in aligned and non-aligned junctions. The arrows denote the binned intensity level group with the highest percentage of cells. Note the shift in population in aligned vs. non-aligned junctions. I) Magnification of a multicellular arc from a mouse lens placode immunolabeled for F-actin

and MyoIIB J) The average relative junctional intensity measured for ZO1, F-Actin and Myosin IIB in aligned and non-aligned junctions (the asterisks indicate $p<\alpha=0.05$). K) Apical view of a Stage II lens placode labeled with SiR-Actin. The yellow bracket indicates the magnified region imaged in time-lapse in (L). L) Still images from a movie of lens placodal cells immunolabeled with SiR-Actin. The yellow arrowheads depict a multicellular arc labeling specific multicellular junctions at different time points of lens invagination. M) The graph indicates the percent of the original length of circumferential junctions from four representative multicellular arcs. N) Working model of lens epithelium invagination: first, multicellular arcs form within the lens placode. Junctional contraction is represented by green arrows along the multicellular arcs. Second, the shortening of the arcs help placodal cells to move toward the center. The red arrows depict the resulting cell movement from circumferential junctional contraction.

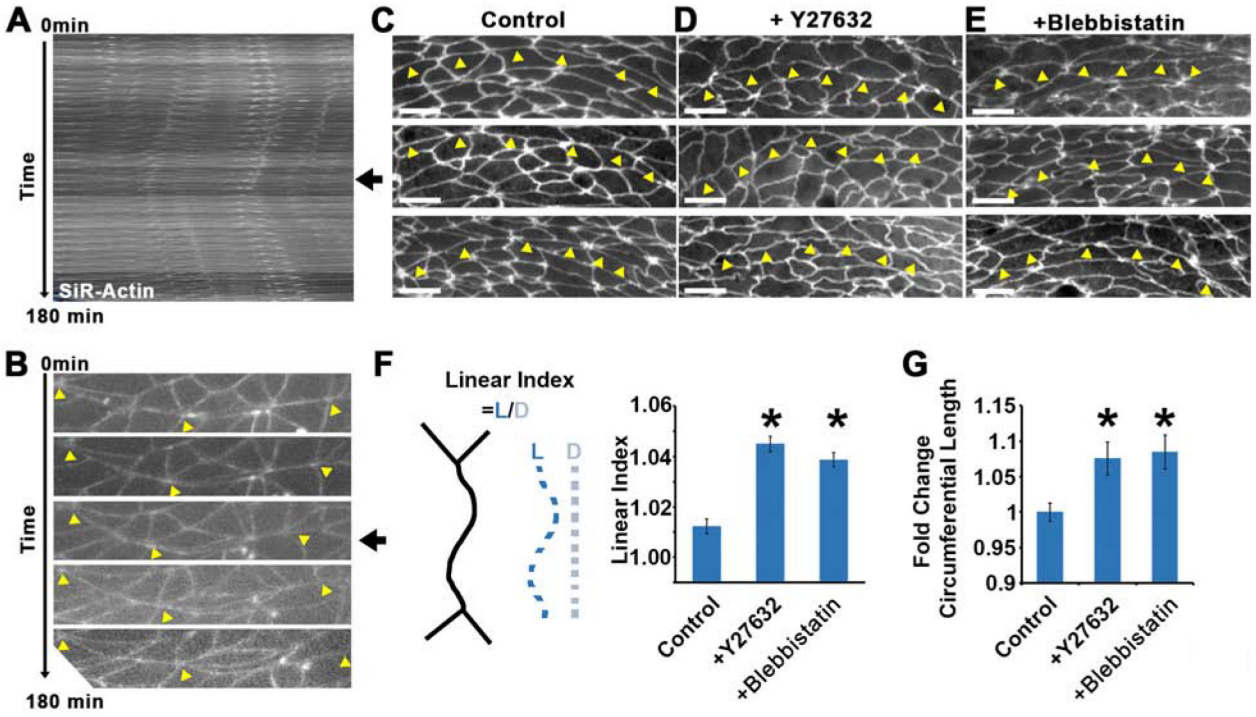

Fig. 3.

(A) Kymograph from a 180 min movie of a SiR-Actin immunofluorescently labeled lens placode treated with Y27632, a Rho-kinase inhibitor. The black arrow indicates the timing of inhibitor addition. (B) Apical views of a multicellular arc from the movie at distinct time points without distortion during the inhibition treatment. The vertices indicated by the yellow arrowheads move further apart after the addition of Y27632 resulting in the lengthening of the junctions. C-E) Apical views of three multicellular arcs from control (C), Y27632 (D) or Blebbistatin (E) treated lens placodes. The yellow arrowheads indicate the multicellular arc in each panel. Note the waviness of junctions in E and F. F) The graph indicates the average linear index, measured as explained in the schematic, of individual circumferentially orientated junctions after inhibition treatment. G) The graph represents the average fold change of the circumferential length for the junctions of these multicellular arcs. Scale bars = 10 μm. Error bars show the standard error and the asterisks indicate $p<\alpha=0.05$.

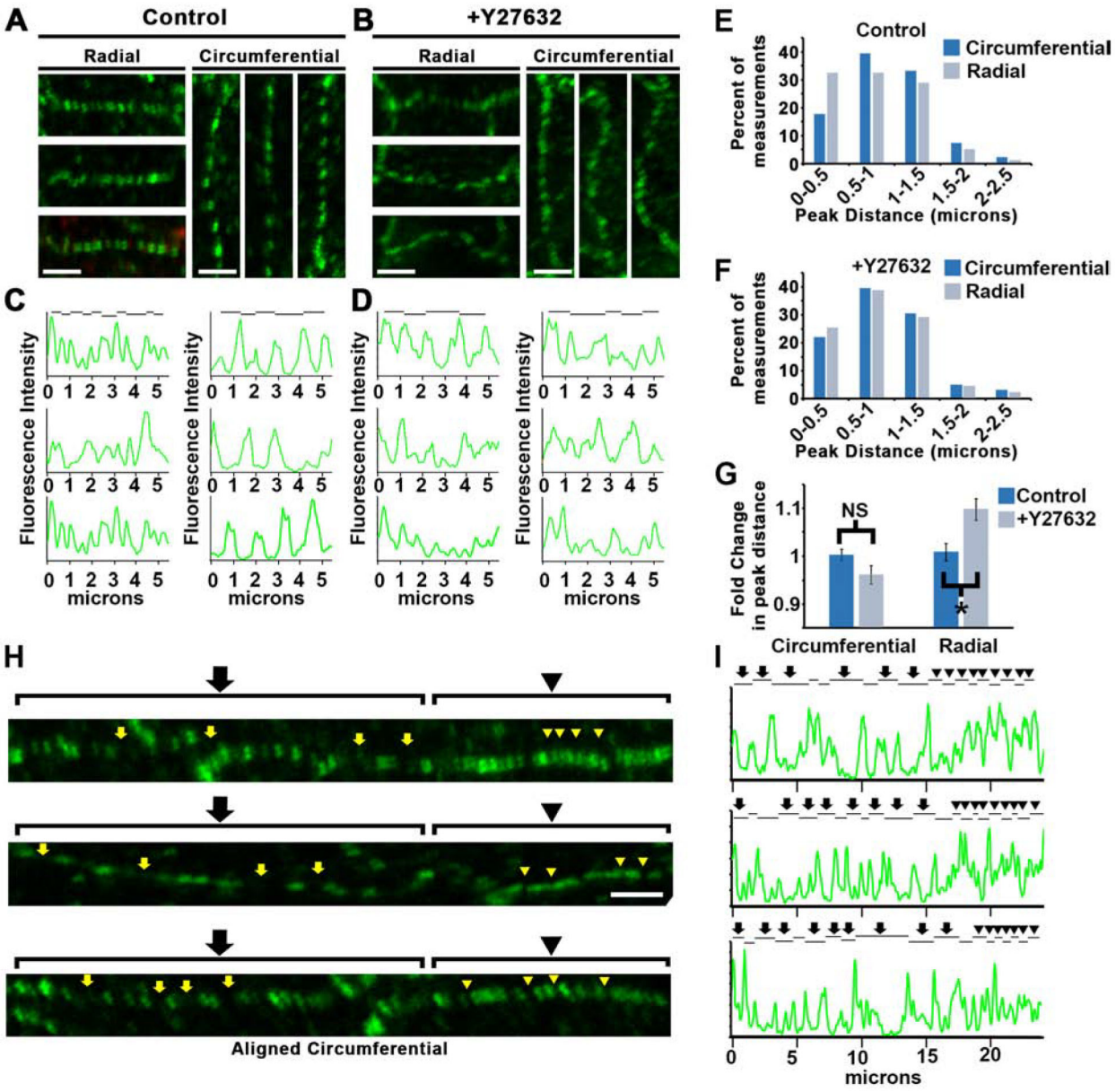

Fig. 4.

A-B) High magnification of three representative, radially and circumferentially orientated placodal junctions immunofluorescently labeled for phospho-myosin light chain (pMLC) from control or rho-kinase inhibitor treated embryos. C-D) Line graphs depicting the fluorescent signal intensity along the junctions shown in A-B. The black lines above each graph indicate the distance between peak intensities that are automatically detected by algorithms in ImageJ (PeakFinder). E-F) Graph of the population distribution of all distance measurements made between peaks of pMLC labeling intensity. Note that difference in population measurements between the circumferential and radial junctions in the control group but not the rho-kinase inhibitor treated group. G) The graph indicates the average of peak intensity measurements in each experimental group. Note that the average radial junction distance increases in the rho-kinase inhibitor treated group suggesting a loss of

contractility and that this is not observed in the non-contracting circumferential junctions. H) Distribution of pMLC along aligned circumferential junctions. Note that the variations in the pMLC puncta spacing (arrows indicating a longer distance and arrowheads indicating a shorter distance) are indicative of its contractile activity. I) Line graphs depicting the pMLC fluorescent signal intensity along the junctions shown in H. The black lines above each graph indicate the distance between peak intensities. Aligned circumferential junctions are contracting regionally as indicated by the distribution of the pMLC puncta. Scale bars = 2 μm. Error bars show the standard error and the asterisks indicate p<=0.05; NS = non-significant.

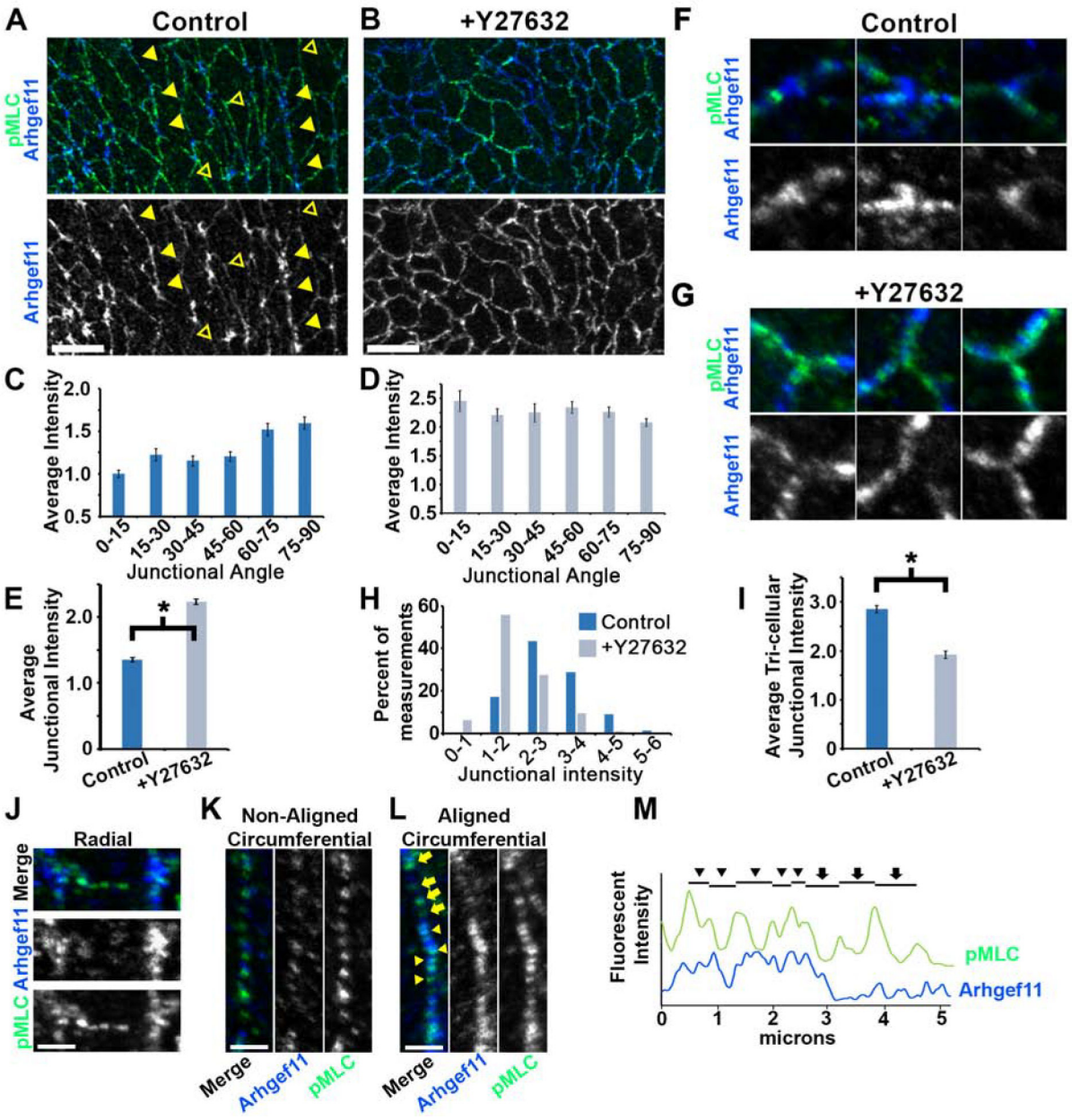

Fig. 5.

(A-B) Apical views of whole-mounted lens placodes immunofluorescently labeled for pMLC (green) and Arhgef11 (blue) in control or rho-kinase inhibitor treated embryos. The center of the placode is left of each image. The closed yellow arrowheads indicate the preferential distribution of Arhgef11 along the circumferential aligned junctions whereas the open arrowheads indicate its absence in other junctions. Note that the anisotropic distribution of Arhgef11 is lost following rho-kinase inhibition treatment. (C-D) The graphs represent the average Arhgef11 signal intensity with respect to the orientation of the junction. The smaller angles indicate junctions orientated more radially, and the larger angles more circumferentially. E) The graph depicts the average signal intensity irrespective of junctional orientation in control or rho-kinase inhibitor treated embryos. (F-G)

Representative examples of Arhgef11 (blue) accumulation at tricellular junctions in control (F) or rho-kinase treated (G) lens placodes. Note that the addition of Y27632 results in a decrease in Arhgef11 signal intensity at the tricellular junctions. H) The graphs indicate the population distribution of signal intensity measurements made for tricellular junctions labeled for Arhgef11 in control or rho-kinase inhibitor treated embryos. Note the shift in population such that there is a higher percentage of cells with more intense junctions in the control group. I) The graph depicts the average tricellular junctional intensity in each experimental group. J-L) Distribution of Arhgef11 (Blue) and pMLC (green) in representative radial (J), non-aligned (K) and aligned (L) circumferential junctions. Arhgef11 is mostly absent from radial (J) and non-aligned (K) junctions whereas it accumulates in aligned circumferential junctions (L, yellow arrowheads). The arrows indicate a region of Arhgef11 absence that correlates with an increase in the distance between pMLC puncta and the arrowheads indicate a region of Arhgef11 presence that correlates with a more densely packed region of pMLC puncta. M) A representative graph showing that the distance between pMLC peaks relative to Arhgef11 localization. Scale bars = 10 μm (A-B) and 2 μm (J-L). Error bars show the standard error and the asterisks indicate $p<0.05$.

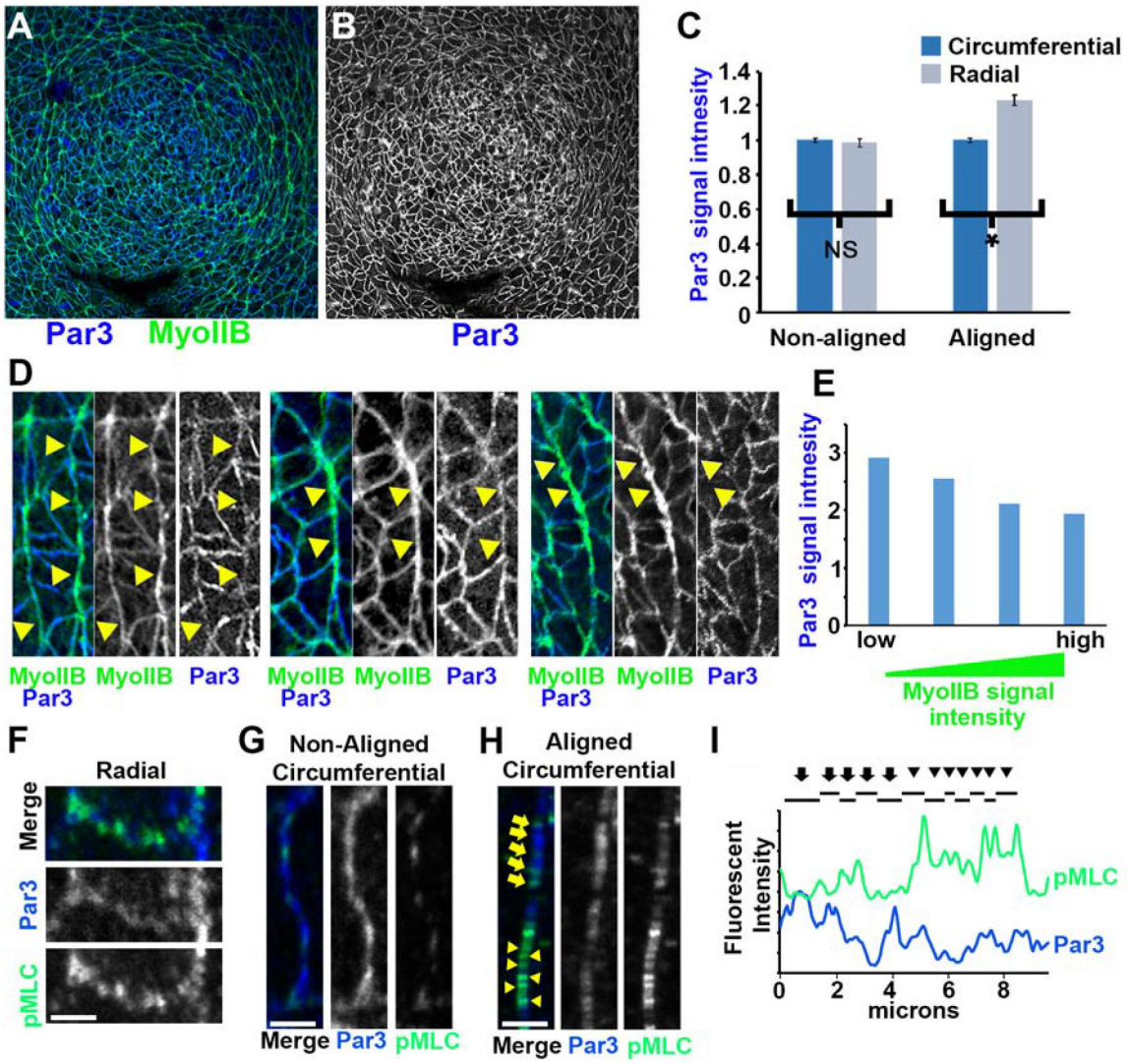

Fig. 6.

A-B) Apical views of whole-mounted chicken lens placodes immunofluorescently labeled for Par3 (blue) and MyoIIB (green). C) The graph illustratesPar 3 signal intensity along the non-aligned and aligned junctions. Note the shift of Par3 in the radial junctions neighboring the aligned junctions. D) Examples of multicellular junctional arcs. The arrowheads indicate the complementary distribution of Par3 and MyoIIB. E) The average Par3 signal intensity along junctions with high or low MyoIIB labeling is depicted. (F-H) Distribution of Par3 (blue) and pMLC (green) in representative radial (F), non-aligned (G) and aligned (H) circumferential junctions. The arrows in H indicate a region of a junction with more intense Par3 labeling in that correlates with an increase in the distance between pMLC puncta and the arrowheads indicate a region of reduced Par3 labeling that correlates with a more densely packed region of pMLC puncta. I) A representative graph showing that the distance between pMLC peaks relative to Par3 localization. Scale bars = 2 μm. Error bars show the standard error and the asterisks indicate $p<0.05$.

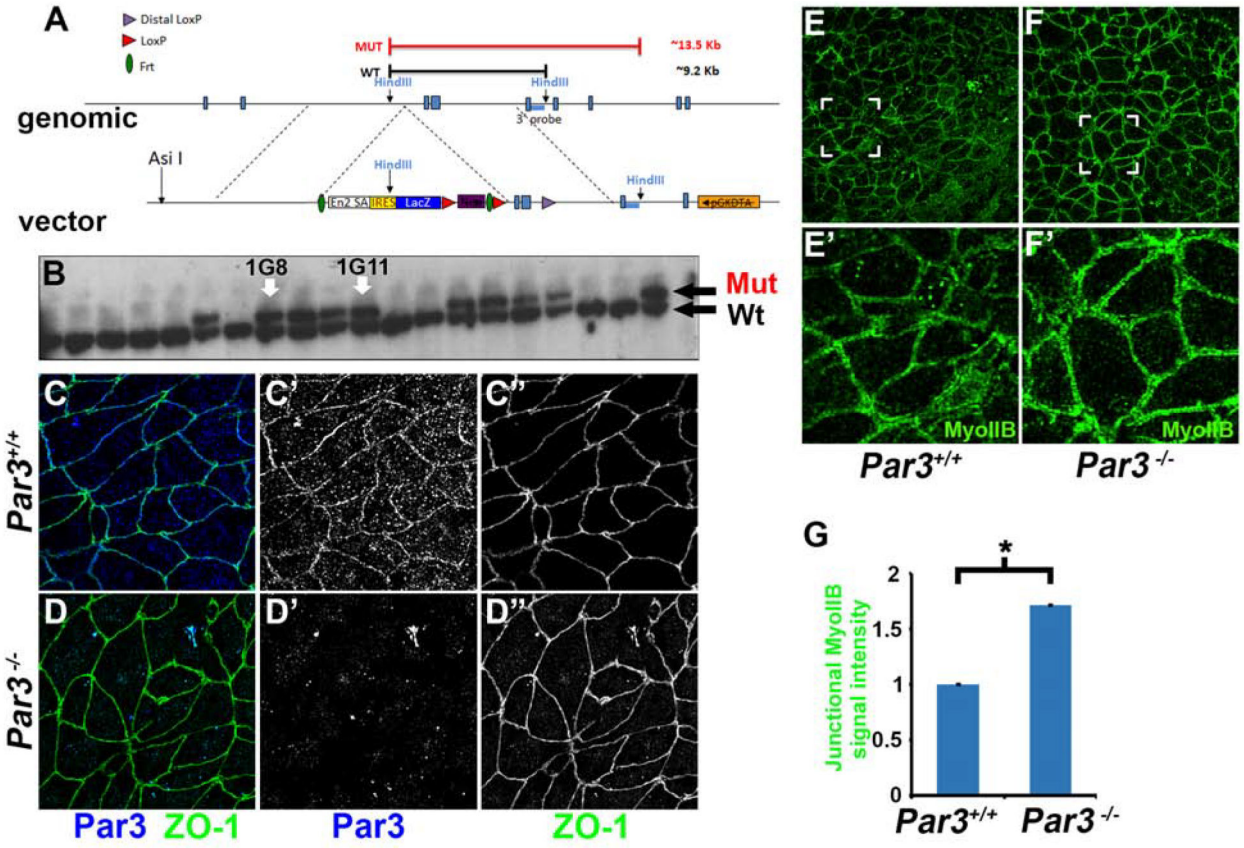

Fig. 7.

A) Diagram of the Pard3 (Par3) targeting vector and the genomic region targeted. Note the location of the Southern probe used in B. B) Southern blot of targeted ES cell clones digested by HindIII. C-D) Apical views of whole-mounted Par3$^{+/+}$ and Par3 $^{-/-}$ mouse lens placodes immunofluorescently labeled for Par3 and ZO-1. Note the lack of junctional Par3 in the Par3 homozygous mutants. E-F) Apical views of whole-mounted Par3$^{+/+}$ and Par3 $^{-/-}$ mouse lens placodes immunofluorescently labeled MyoIIB (green). E) The graph indicates the average MyoIIB junctional signal intensity in placodes from each genotype. Note that it is significantly increased in Par3 deficient lens placode. Error bar show the standard error and the asterisks indicate $p<0.05$.

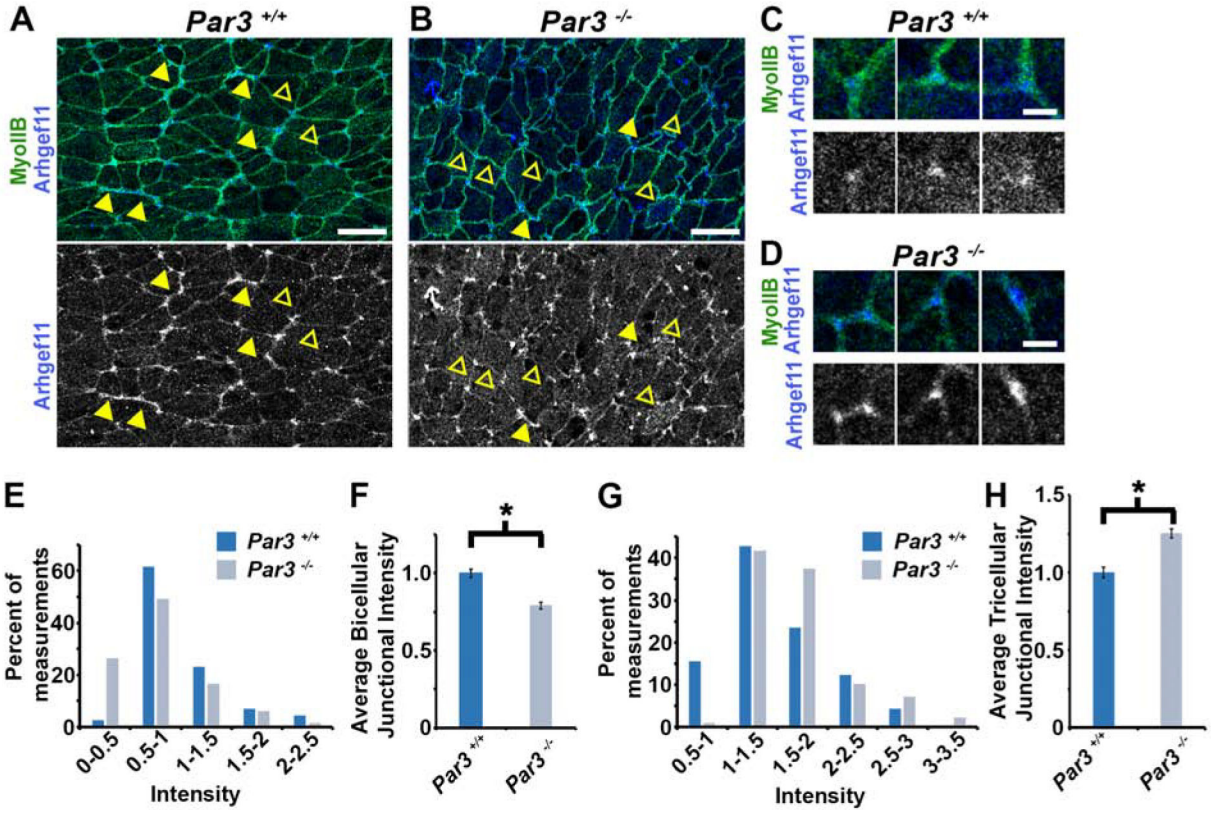

Fig. 8.

(A-B) Apical views of whole-mounted control or Par3-deficient mouse lens placodes immunofluorescently labeled for Arhgef11 (blue) and MyoIIB (green). The closed arrowheads point junctions where Arhgef11 is accumulated whereas the open arrowheads indicate junctions where Arhgef11 is absent. C-D) Higher magnification of three representative tricellular junctions labeled as in A-B from control or Par3 deficient embryos. E-H) The graphs depict the population distribution of intensity measurements (E,G) or average intensity of all measurements (F,H) of Arhgef11 in bicellular (E-F) or tricellular (G-H) junctions from control or Par3-deficient embryonic placodes. Note that the shift in Arhgef11 intensity between genotypes in bicellular vs. tricellular junctions are complementary. Scale bars = (A-B) 10 μm and (C-D) 2 μm. Error bars show the standard error and the asterisks indicate $p<0.05$.

REAGENT or RESOURCE	SOURCE	IDENTIFIER
Antibodies		
Rabbit anti-β-catenin	Santa Cruz	Cat # sc-7199
Mouse anti-β-catenin	Biosciences	Cat# 610153
Rabbit anti-myosin IIb	Covance	Cat# PRB445P
Mouse anti-myosin IIB	DSHB	Cat # CMII 23-s
Mouse anti-Phospho-Myosin Light Chain 2 (Ser19)	Cell Signaling Technology	Cat #3675S
Rabbit Par3	Millipore	Cat #07–330
Rabbit anti-Arhgef11	Atlas Antibodies	Cat # HPA01126
Rabbit anti-Prox1	EMD Millipore	Cat # AB5475
Phalloidin 488	Invitrogen	Cat # A12379
Hoechst 33342	Sigma	Cat # B-2261
Biological Samples		
Chicken embryos lens placodes	This paper	N/A
Par3 deficient Mouse lens placodes	This paper	N/A
DNA vector		
KOMP-PRPGS00162_B_E11-Pard3	KOMP	N/A
Chemicals, Peptides, and Recombinant Proteins		
Y-27632	EMD Millipore	Cat# 688001–500μg
Blebbistatin	EMD Millipore	Cat# 203389–5MG
SiR-Actin	Cytoskeleton, Inc	Cat # SC001
Oligonucleotides		
Primer: 5’-GGGATCTCATGCTGGAGTTCTTCG-3’ (KO)	This paper	N/A
Primer: 5’-TCCCAGCTGCTTAATCGAGGCCATCA-3’ (KO)	This paper	N/A
Primer: 5’-CCAATT ATCGGACTGTAGAATT GT GA-3’(wt)	This paper	N/A
Primer: 5’-AGTTACACTGGGAAGACCACCACAGT-3’ (wt)	This paper	N/A
Software and Algorithms		
Image J – Peak finder tool	https://imagej.nih.gov/ij/	N/A
Zen 2012	Zeiss	N/A
MIPAR	https://www.mipar.us/	N/A
Experimental Models: Organisms/Strains		
Chicken embryos	Michigan State University Poultry Farm Charles Rivers	N/A
Par3 deficient Mouse embryos (see Materials and methods	This paper	N/A